

Enhanced hydrodynamic diffusion in dense binary active suspensions

Zhouyang Ge^{1,2}, Shervin Bagheri¹, and Gwynn J. Elfring²

¹*FLOW, Department of Engineering Mechanics, KTH Royal Institute of Technology, 100 44 Stockholm, Sweden and*

²*Department of Mechanical Engineering and Institute of Applied Mathematics, University of British Columbia, Vancouver V6T 1Z4, BC, Canada*

We study the effect of incorporating passive particles into a dense active suspension. Specifically, we focus on individually immotile active particles, or shakers, whose collective dynamics arise from the activity-induced many-body hydrodynamic interactions. In the absence of Brownian motion, both active and passive particles fluctuate vigorously in space, displaying pronounced hydrodynamic diffusion. The rotational diffusivity of all particles decreases monotonically with the fraction of passive ones; however, surprisingly, the translational diffusivity is nonmonotonic and can be significantly enhanced. This suggests a hydrodynamic coupling of the translational and rotational dynamics, which we find can be attributed to local ordering of the active particles as a result of hydrodynamic interactions. Using a toy model, where passive particles are treated as defects in a lattice of aligned force dipoles, we reveal a simple mechanism by which spatial correlations and inactivity give rise to enhanced diffusion. Our results uncover an unexpected effect of passive particles on the dynamics of active suspensions, providing new possibilities to enhance mixing and modulate mass transport in active fluids.

Flowing suspensions of non-Brownian particles often display stochastic diffusive-like dynamics known as *hydrodynamic diffusion* [1]. Common examples include sheared suspensions, where particles driven by an externally imposed velocity gradient undergo chaotic and anisotropic displacements [2, 3], and sedimentation, where long-range velocity correlations result in tortuous and loopy falling paths [4]. The apparent random motion arises not from thermal fluctuations but rather the flow-induced multiparticle interactions, determined by the relative positions and orientations of many particles, leading to complex dynamics.

Suspension dynamics may be more complex if the particles are *self-driven*, expending and dissipating energy at the microscale [5]. In a seminal experiment, Wu and Libchaber [6] studied particle diffusion in a quasi-two-dimensional bacterial bath. Suspending trace amounts of micron-sized polystyrene spheres in a soap film with concentrated *E. coli* bacteria, they observed short-time superdiffusion and long-time diffusion of the tracers. The effective diffusion coefficient increased linearly with bacterial concentration and was 2–3 orders of magnitude higher than what it would be without the bacteria. Bacterial dynamics have since been shown to exhibit large-scale coherence [7, 8], novel orientational instabilities [9, 10] and rheology (e.g. vanishing viscosity under shear) [11, 12], and numerous studies have greatly improved our understanding of particle transport in active fluids [13–34]. Recent studies have shown non-Gaussian statistics of the particle displacements in dilute active suspensions [17–21], identified a proportionality between the enhanced diffusion and the active cell flux [22–26], and the effects of tracer particle size [27, 35] and shape [28–30]. Previous studies considered the effect of active particles on the diffusion of passive tracers in relatively dilute suspensions, usually less than 15% by volume. The *converse*

question on the effect of passive particles on active particles at *high* concentrations has yet to be explored. This is of great practical relevance, since any realistic active system, biological or synthetic, almost always contains some passive components (e.g. dead cells or defects). In addition, the active particles employed in previous studies were always self-propelling, thus excluding active but non-self-propelling particles such as melanocytes in the skin [36], or bacteria in crowded environments [37].

In this Letter, we report large-scale hydrodynamic simulations on the effect of passive particles on the dynamics of dense active suspensions. Specifically, we study *shakers* – particles that are active but *not* self-propelling. The numerical method we use accounts for both hydrodynamic and excluded-volume interactions amongst the particles, necessary for correctly capturing their dynamics at the volume fractions we consider (40% and 50%). Extensive simulations of up to 4096 particles show that the suspensions always reach steady states characterized by a random spatial distribution of active and passive particles, with the same kinetic energy. Furthermore, all particles display diffusive translational dynamics at long times, allowing for an effective diffusivity D to be calculated. Surprisingly, D is *nonmonotonic* in the fraction of passive particles f_p : a peak diffusivity is obtained when 10–50% of the particles are passive. The rotational diffusivity D_r , on the other hand, decreases with f_p . The different behaviors of D and D_r result from an activity-induced local ordering of the shakers, which in the presence of passive particles gives rise to the enhanced D . We illustrate this purely hydrodynamic mechanism by a toy model, where passive particles are treated as defects in a lattice of symmetric force dipoles, or stresslets. Our results reveal an unexpected effect of inactive particles on active hydrodynamic diffusion, offering new strategies to enhance mixing and transport (by turning *off* activity)

in dense active matter [38].

Models and methods.—We model active particles as “squirmers,” spheres with a prescribed axisymmetric slip velocity [39–41]. Following Ref. [42], the active slip velocity at position \mathbf{r} from the sphere’s center may be expressed as $\mathbf{u}_s = \mathbf{U}_s + \boldsymbol{\Omega}_s \times \mathbf{r} + \mathbf{E}_s \cdot \mathbf{r} + \dots$, where \mathbf{U}_s is the self-propulsion velocity of the squirmer, $\boldsymbol{\Omega}_s$ the self spin, \mathbf{E}_s the self strain rate, and dots denote terms involving higher order irreducible tensors of \mathbf{r} [42]. Specifically, $\mathbf{U}_s = \frac{2}{3} B_1 \mathbf{p}$, $\boldsymbol{\Omega}_s = \frac{C_1}{a^3} \mathbf{p}$, $\mathbf{E}_s = -\frac{3}{5} \frac{B_2}{a} (\mathbf{p}\mathbf{p} - \frac{1}{3} \mathbf{I})$, where B_1 and B_2 are the so-called squirming modes, C_1 a coefficient associated with azimuthal slip, \mathbf{p} a unit vector along the particle axis, and a the particle radius. Setting $B_1 = 0$ yields an immotile squirmer known as a *shaker*.

Although shakers are individually immotile, they swim *collectively* due to hydrodynamic interactions (HIs). To leading order, the HIs arise from \mathbf{E}_s if $B_2 \neq 0$: $B_2 > 0$ corresponds to pullers, while $B_2 < 0$ pushers. The ratio $\beta \equiv B_2/B_1$ thus differentiates the type of swimmer and indicates the relative importance of HIs and self-propulsion. In this work, we focus on shakers, i.e. $|\beta| \rightarrow \pm\infty$, to amplify the effect of HIs, except in one contrasting case where we set $\beta = 0$, corresponding to neutral “movers.” Higher-order squirming modes are neglected, and azimuthal slip is not considered, as is common in the literature [16, 43, 44]. In our description the prescribed velocity is given simply by $\mathbf{u}_s = \mathbf{U}_s + \mathbf{E}_s \cdot \mathbf{r}$, which is not purely tangential, and a suspension of movers do not interact hydrodynamically due to self-propulsion, behaving effectively as active Brownian particles (ABPs) in our simulations, as interactions due to B_1 appear at higher order [42].

The dynamics of a suspension of shakers are computed using the Fast Stokesian Dynamics (FSD) method [45], which is modified for active particles [42]. See Ref. [46] for further numerical validation of FSD in sheared passive suspensions. Specifically, we simulate binary suspensions of shakers, pulling (S_+) or pushing (S_-) types, with various fractions of passive (P) particles, $f_p \in [0, 1]$, in three dimensions (3D) with periodic boundary conditions. Combinations of movers (M) and passive particles, as well as of the two shakers (S_+, S_-), are also considered for comparison. Two volume fractions, $\phi = 40\%$ and 50% , and two sample sizes, $N = 1024$ and 4096 , are examined; see the supplemental material (SM) for a summary of all simulated cases and the detailed computational setup and solver verifications.

Spatial and energy distributions.—First, we examine the spatial distribution of the particles. Visual inspections suggests that the two groups of particles are always mixed, see Fig. 1(a) inset. The extent of mixing can be quantified by the probability $\rho_k^{(ij)}$ of any particle in group i to find its k nearest neighbours to *all* belong to group $j \neq i$; $i, j = 1$ or 2 representing active and passive particles respectively. If the two groups of particles are

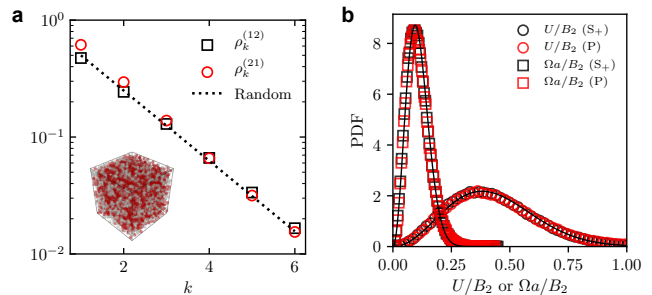


Figure 1: Spatial and energy distributions in an (S_+, P) suspension; $f_p = 0.5$, $\phi = 40\%$. (a) Probability $\rho_k^{(ij)}$ that a particle in group i finds its first k nearest neighbors all in group j ; the dotted line denotes the random distribution. Inset shows a snapshot of the suspension. (b) Distribution of the particle speeds, where lines are fits to the Maxwell-Boltzmann distribution.

randomly distributed, we would expect $\rho_k^{(ij)} \approx f_j^k$, where f_j is the fraction of particles in group j . This is indeed observed, see Fig. 1(a) for an example and SM for further details.

Next, we examine the energy partition in our suspensions. The mean translational and rotational energies per particle, proportional to U_{rms}^2 and Ω_{rms}^2 , respectively, are nearly the same among shakers and passive particles (see SM). The equal distribution of kinetic energies is surprising; it implies that the energy exchange between particles may be modelled by an effective collision [6], leading to the emergent equilibrium-like behavior. Indeed, the particle speeds also satisfy the Maxwell-Boltzmann distribution, see Fig. 1(b) [6, 27]. However, the ratio of the linear and angular velocities does not obey equipartition of energy, which would lead to $U_{rms}/(\Omega_{rms}a) = \sqrt{2/5}$; here, $U_{rms} > \Omega_{rms}a$. This suggests that the translational and rotational degrees of freedom are *not* independent, and HIs are at play.

Translational dynamics.—To measure the translational dynamics, we calculate the mean square displacement (MSD), $\langle \Delta r^2(t) \rangle \equiv \langle [\mathbf{r}(\tau+t) - \mathbf{r}(\tau)]^2 \rangle$, of all particles based on their positions $\mathbf{r}(t)$, where $\langle \cdot \rangle$ is an average over both time (τ) and particles. The results exhibit crossovers from short-time ballistic to long-time diffusive dynamics. Assuming a collisional force with zero mean and an exponential autocorrelation between the particles, Wu and Libchaber [6] derived an analytical expression for the MSD, $\langle \Delta r^2(t) \rangle = 6Dt(1 - e^{-t/t_c})$, where D is the diffusion coefficient and t_c the crossover time. Rescaling time by t_c and the MSD by $6Dt_c$ collapses all our data, as shown in Fig. 2(a). Although our data mainly fall in the ballistic regime (due to the computational box size), we have checked that even in short times ($t \ll t_c$) the probability distributions of the particle displacements have finite variance (see SM), thus the dynamics will become

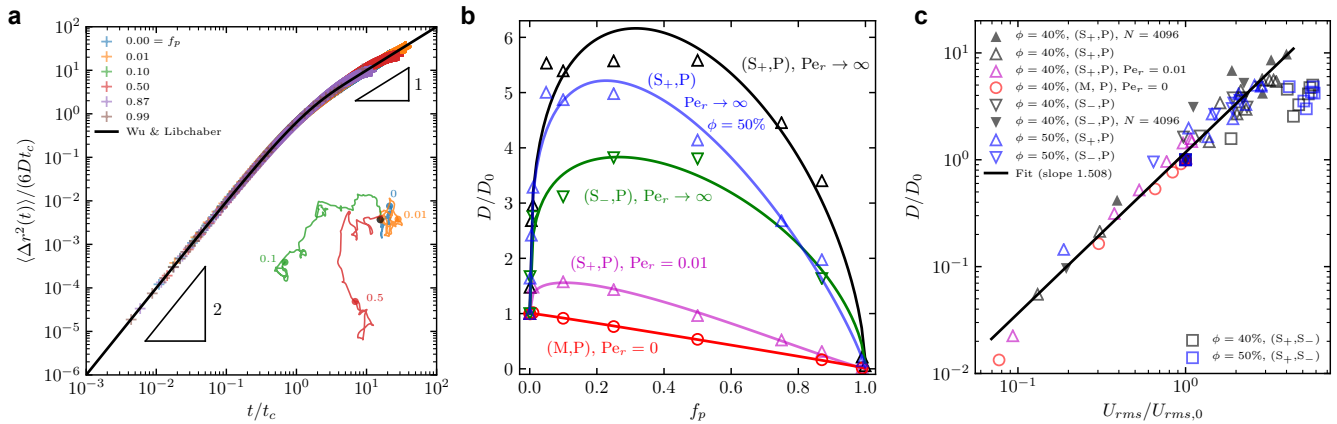


Figure 2: Translational dynamics. (a) MSD of the (S_+,P) suspension at different f_p ($\phi = 40\%$); inset shows the projected trajectory of a shaker (labelled by f_p). (b) Relative diffusivity, D/D_0 , as a function of f_p for five representative suspensions, where lines are least squares fits of the form $y = ax^{\nu_1}(1-x)^{\nu_2} + 1 - x$ (see text for the definition of Pe_r and SM for the full results). (c) Relationship between long-time and short-time dynamics, where the solid line is a least square fit of the data excluding the (S_+,S_-) suspensions.

diffusive per the central limit theorem.

Strikingly, shakers fluctuate *more* in the presence of passive particles; see Fig. 2(a) inset and supplemental videos. Fig. 2(b) shows D versus fraction of passive particles f_p relative to D_0 at $f_p = 0$ for a few representative cases. We find, in all cases (except movers), an enhancement of diffusivity with an increase with f_p until reaching a peak before declining necessarily to $D = 0$ at $f_p = 1$. The diffusivity of active-active mixtures, (S_+,S_-) , is also greater than those of pulling or pushing shakers alone (see SM); and we note that the short- and long-time dynamics are positively correlated, see Fig. 2(c). The latter implies that the translational dynamics are characterized by a *single* timescale, a/U_{rms} , which is related to t_c as both arise from HIs (see SM). Moreover, the effects of the volume fraction, sample size, and type of shakers appear to be weak, thus the dynamics enhancement is robust. The only instance where we observe a qualitative difference is with suspensions of movers (M,P): their diffusive dynamics monotonically decay with the volume fraction of passive particles; however, since movers do not generate activity induced flows in our model, this indicates that the enhanced dynamics in shakers must be due to hydrodynamic interactions.

Rotational dynamics.—Given the importance of hydrodynamic interactions, we examine the rotational dynamics as they are coupled to the translational ones. Fig. 3(a) shows the autocorrelation of the particle orientation, $\langle \mathbf{n}_0 \cdot \mathbf{n}_t \rangle$, for (S_+,P) suspensions at different f_p . The exponential decay of $\langle \mathbf{n}_0 \cdot \mathbf{n}_t \rangle$ defines the rotational diffusivity D_r [47]; here, D_r stems solely from HIs and reduces with f_p . Particle reorientation may also occur due to non-hydrodynamic (e.g. biological) mechanisms, which can be simply modelled as a white noise in the

angular velocity (see SM) [48]. The relative strength of the reorientation mechanisms can then be quantified by a rotational Péclet number, $Pe_r \equiv D_r/\nu_r$, where ν_r is the angular diffusivity associated with the prescribed noise.

Plotting the relative rotational diffusivity, $D_r/D_{r,0}$, at different Pe_r clearly shows different behavior compared to the translational diffusivity [see Figs. 2(b) and 3(b)]. While D is nonmonotonic with f_p (for $Pe_r > 0$), D_r reduces monotonically with f_p . Conversely, when $Pe_r = 0$, D reduces monotonically with f_p while D_r is relatively unchanged. These observations, combined with the unequal energy partition [c.f. Fig. 1(b)], are clear signatures of the hydrodynamic coupling of translational and rotational diffusivities, which further implies spatial correlations in our suspensions.

Spatial correlations.—Long-range nematic order is known to be absolutely unstable in apolar active sus-

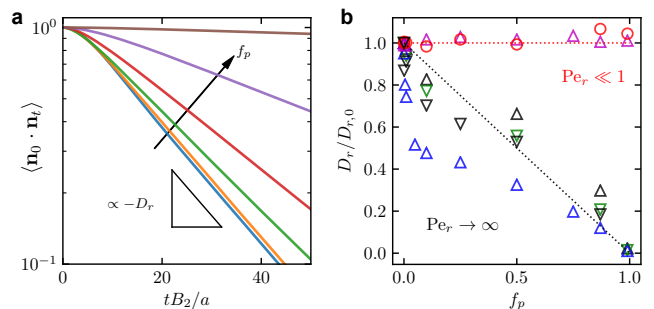


Figure 3: Rotational dynamics. (a) Autocorrelation of the particle orientations in (S_+,P) suspensions at $\phi = 40\%$. (b) Relative rotational diffusivity, $D_r/D_{r,0}$, for five representative suspensions; c.f. Fig. 2(b).

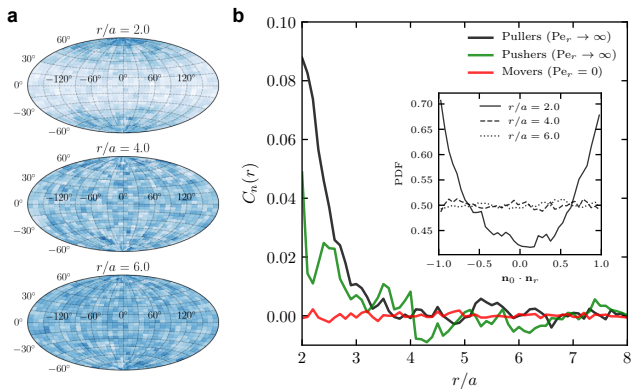


Figure 4: Spatial correlations. (a) Angular distributions at $r/a = 2, 4, 6$ for suspensions of pulling shakers; $f_p = 0$, $\phi = 40\%$. The maps are oriented such that the particle axis \mathbf{p} goes through the north and south poles (Aitoff projection). (b) Orientation correlations in suspensions of pullers, pushers and movers; inset shows the probability distribution of $\mathbf{n}_0 \cdot \mathbf{n}_r$ for pullers.

pensions [9]. For shakers, this was shown to result in an isotropic global orientation distribution [49], which we confirm in our simulations (see SM). To examine short-range order, we calculate the pair correlation function, $g(r) = \sum_{i \neq j}^N \langle \delta(r - r_{ij}) \rangle / (4\pi r^2 N \rho)$, where ρ is the particle number density and $\langle \cdot \rangle$ a time average. $g(r)$ displays the typical oscillatory behavior with decaying peaks at $r/a \approx 2, 4, 6$, and so on, corresponding to the first few particle layers in a hard sphere liquid. However, the angular distribution near the first particle layer, $r/a = 2$, is not isotropic: pulling shakers tend to find their nearest neighbors along the particle axis \mathbf{p} , whereas pushing shakers tend to find them in the plane perpendicular to \mathbf{p} ; see Fig. 4(a) and SM. Furthermore, since the same correlation applies also to the neighbors, adjacent shakers must be approximately aligned: for pullers, the alignment is head-to-head; for pushers, it is side-by-side. Fig. 4(a) shows that the spatial ordering does not extend beyond the first particle layer.

To quantify the alignment, we define a correlation function for the particle orientation, $C_n(r) = 2\langle |\mathbf{n}_0 \cdot \mathbf{n}_r| \rangle - 1$, where $\langle \cdot \rangle$ is an average over all particles and time; $C_n(r) = 0$ if there is no correlation, and $C_n(r) = 1$ if there is maximal nematic order. Fig. 4(b) shows that there is indeed a local alignment (with a $\mathbf{n} \rightarrow -\mathbf{n}$ symmetry; see PDFs in the inset) for pulling and pushing shakers up to $r/a \approx 4$, consistent with what we inferred from the angular distributions. In contrast, movers and particles with strong angular noise, display no such order at any r . Similar local ordering was observed in suspensions of self-locomoting rods [37, 50], our results show that spheres can also be aligned due to hydrodynamic interactions.

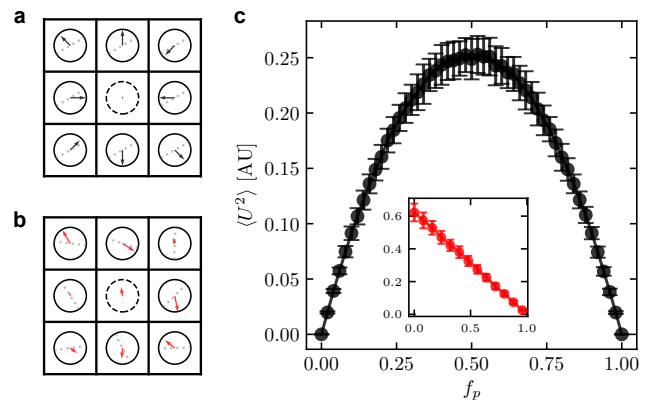


Figure 5: Toy model. (a,b) Illustrations of active (circles oriented along the gray dotted lines) and passive particles (dashed circles in the center) on a square lattice; perfect alignment in (a), random orientation in (b). The arrows denote the activity-induced velocities. (c) Mean square velocity $\langle U^2 \rangle$ in arbitrary units as a function of f_p obtained from 100 periodic lattices of 100 particles; the active particles are aligned in the main plots but oriented randomly in the insets.

Toy model.—We now propose a simple toy model to explain the enhanced dynamics in binary active suspensions. Consider a two dimensional (2D) square lattice of force dipoles (stresslets), as shown in Fig. 5(a,b). Each generates a flow field proportional to $|B_2|/r^2$, and we assume that the flow only affects the first layer of neighboring particles. Passive particles are modeled as *defects*, i.e. they are affected by nearby flows but produce no flow in return (the reflected flow would be a higher order effect). Superposition of the induced flow yields the total velocity on each particle per spatial arrangement. Repeated sampling then generates the mean square velocity, $\langle U^2 \rangle$, at a fixed f_p . The idea is to link the diffusion to microstructure via $\langle U^2 \rangle$, since we know that short- and long-time dynamics are correlated.

The results of the toy model are shown in Fig. 5(c). We can see that $\langle U^2 \rangle$ peaks at $f_p = 0.5$ when the dipoles are aligned, but decreases monotonically with f_p in the absence of alignment; both are observed in the full simulations, c.f. Fig. 2(b). This suggests a very simple mechanism for the observed nonmonotonic dynamics: active particles aligned in the near field generate flows that cancel out, thus the *net* flow can be increased by passive particles that disrupt this symmetry. Given the simplicity of the model, the agreement is remarkable and implies that the essential physics is largely captured and suggests new strategies to modulate particle transport and mixing by controlling individual particle (in)activity [38]. Restricting particles on a square periodic lattice in perfect alignment is of course an idealization; but the same effect would be observed in any lattice with reflection and

twofold symmetries, and we have checked that adding a small amount of noise in the particle positions or orientations does not change the results qualitatively (see SM).

One may question whether the dynamic enhancement observed here persists if the active particles are self-propelling. At lower volume fractions we expect substantially different physics; however, at high volume fractions self-propulsion can lead to phase separation [51], where particles cluster and experience reduced motility, and in that case, passive particles may lead to dynamic enhancement and cluster destabilization. Another important question concerns the effects of particle shape and boundaries. Many natural microswimmers (e.g. *E. coli*) are elongated, which tend to accumulate near walls and swim collectively or form biofilms [52]. Steric interactions between anisotropic particles will certainly affect rotational dynamics, and this is further complicated by the presence of boundaries or confinement. Although the asymptotic scaling of the flows near walls differs [53], the symmetry of the flow in the wall-parallel direction is unchanged and so we should expect similar results if the active particles are aligned locally, which is indeed observed in experiments of filamentous bacteria in thin films [37]. Finally, real active systems will generally contain some fraction of inactive particles [24, 25], and any enhancement of diffusivity will depend on the various physical parameters in different active suspensions

The authors wish to thank R. Vallon, L. Brandt, S. S. Ray, H. Diamant, J.-L. Thiffeault, and S. Guo for useful discussions. Z.G. acknowledges support from the Swedish Research Council under Grant No. 2021-06669VR.

-
- [1] R. H. Davis, *J. Fluid Mech.* **310**, 325 (1996).
 [2] G. Drazer, J. Koplik, B. Khusid, and A. Acrivos, *J. Fluid Mech.* **460**, 307–335 (2002).
 [3] D. J. Pine, J. P. Gollub, J. F. Brady, and A. M. Leshansky, *Nature* **438**, 1476 (2005).
 [4] É. Guazzelli and J. Hinch, *Ann. Rev. Fluid Mech.* **43**, 97 (2011).
 [5] S. Ramaswamy, *J. Stat. Mech.: Theory Exp.* **2017**, 054002 (2017).
 [6] X.-L. Wu and A. Libchaber, *Phys. Rev. Lett.* **84**, 3017 (2000).
 [7] C. Dombrowski, L. Cisneros, S. Chatkaew, R. E. Goldstein, and J. O. Kessler, *Phys. Rev. Lett.* **93**, 098103 (2004).
 [8] A. Sokolov, I. S. Aranson, J. O. Kessler, and R. E. Goldstein, *Phys. Rev. Lett.* **98**, 158102 (2007).
 [9] R. A. Simha and S. Ramaswamy, *Phys. Rev. Lett.* **89**, 058101 (2002).
 [10] D. Saintillan and M. J. Shelley, *Phys. Rev. Lett.* **100**, 178103 (2008).
 [11] H. M. López, J. Gachelin, C. Douarche, H. Auradou, and E. Clément, *Phys. Rev. Lett.* **115**, 028301 (2015).
 [12] D. Saintillan, *Ann. Rev. Fluid Mech.* **50**, 563 (2018).
 [13] M. J. Kim and K. S. Breuer, *Phys. Fluids* **16**, L78 (2004).
 [14] D. T. N. Chen, A. W. C. Lau, L. A. Hough, M. F. Islam, M. Goulian, T. C. Lubensky, and A. G. Yodh, *Phys. Rev. Lett.* **99**, 148302 (2007).
 [15] P. T. Underhill, J. P. Hernandez-Ortiz, and M. D. Graham, *Phys. Rev. Lett.* **100**, 248101 (2008).
 [16] T. Ishikawa, J. T. Locsei, and T. J. Pedley, *Phys. Rev. E* **82**, 021408 (2010).
 [17] K. C. Leptos, J. S. Guasto, J. P. Gollub, A. I. Pesci, and R. E. Goldstein, *Phys. Rev. Lett.* **103**, 198103 (2009).
 [18] H. Kurtuldu, J. S. Guasto, K. A. Johnson, and J. P. Gollub, *Proc. Natl. Acad. Sci. U.S.A.* **108**, 10391 (2011).
 [19] J.-L. Thiffeault, *Phys. Rev. E* **92**, 023023 (2015).
 [20] L. Ortlieb, S. Rafai, P. Peyla, C. Wagner, and T. John, *Phys. Rev. Lett.* **122**, 148101 (2019).
 [21] K. Kanazawa, T. G. Sano, A. Cairoli, and A. Baule, *Nature* **579**, 364 (2020).
 [22] Z. Lin, J.-L. Thiffeault, and S. Childress, *J. Fluid Mech.* **669**, 167–177 (2011).
 [23] D. O. Pushkin and J. M. Yeomans, *Phys. Rev. Lett.* **111**, 188101 (2013).
 [24] G. Miño, T. E. Mallouk, T. Darnige, M. Hoyos, J. Dauchet, J. Dunstan, R. Soto, Y. Wang, A. Rousselet, and E. Clement, *Phys. Rev. Lett.* **106**, 048102 (2011).
 [25] A. Jepsen, V. A. Martinez, J. Schwarz-Linek, A. Morozov, and W. C. K. Poon, *Phys. Rev. E* **88**, 041002(R) (2013).
 [26] A. Morozov and D. Marenduzzo, *Soft Matter* **10**, 2748 (2014).
 [27] A. E. Patteson, A. Gopinath, P. K. Purohit, and P. E. Arratia, *Soft Matter* **12**, 2365 (2016).
 [28] Y. Peng, L. Lai, Y.-S. Tai, K. Zhang, X. Xu, and X. Cheng, *Phys. Rev. Lett.* **116**, 068303 (2016).
 [29] O. Yang, Y. Peng, Z. Liu, C. Tang, X. Xu, and X. Cheng, *Phys. Rev. E* **94**, 042601 (2016).
 [30] F. von Rűling, F. Kolley, and A. Eremin, *Colloid Polym. Sci.* **299**, 289 (2021).
 [31] E. W. Burkholder and J. F. Brady, *Phys. Rev. E* **95**, 052605 (2017).
 [32] L. Abbaspour and S. Klumpp, *Phys. Rev. E* **103**, 052601 (2021).
 [33] O. Granek, Y. Kafri, and J. Tailleur, *Phys. Rev. Lett.* **129**, 038001 (2022).
 [34] Y. Kogure, T. Omori, and T. Ishikawa, *J. Fluid Mech.* **971**, A17 (2023).
 [35] T. V. Kasyap, D. L. Koch, and M. Wu, *Phys. Fluids* **26**, 081901 (2014).
 [36] A. Baskaran and M. C. Marchetti, *Proc. Natl. Acad. Sci. U.S.A.* **106**, 15567 (2009).
 [37] H. Li, X.-q. Shi, M. Huang, X. Chen, M. Xiao, C. Liu, H. Chaté, and H. Zhang, *Proc. Natl. Acad. Sci. U.S.A.* **116**, 777 (2019).
 [38] Y. Fu, H. Yu, X. Zhang, P. Magaretti, V. Kishore, and W. Wang, *Micromachines* **13**, 295 (2022).
 [39] M. J. Lighthill, *Commun. Pure Appl. Math.* **5**, 109 (1952).
 [40] J. R. Blake, *J. Fluid Mech.* **46**, 199 (1971).
 [41] T. J. Pedley, *IMA Journal of Applied Mathematics* **81**, 488 (2016).
 [42] G. J. Elfring and J. F. Brady, *J. Fluid Mech.* **952**, A19 (2022).
 [43] T. Ishikawa, M. Simmonds, and T. J. Pedley, *J. Fluid Mech.* **568**, 119 (2006).

- [44] B. Delmotte, E. E. Keaveny, E. Climent, and F. Plouraboué, *IMA J. Appl. Math.* **83**, 680 (2018).
- [45] A. M. Fiore and J. W. Swan, *J. Fluid Mech.* **878**, 544 (2019).
- [46] Z. Ge and G. J. Elfring, *Phys. Rev. E* **106**, 054616 (2022).
- [47] J. R. Howse, R. A. L. Jones, A. J. Ryan, T. Gough, R. Vafabakhsh, and R. Golestanian, *Phys. Rev. Lett.* **99**, 048102 (2007).
- [48] Y. Fily and M. C. Marchetti, *Phys. Rev. Lett.* **108**, 235702 (2012).
- [49] A. A. Evans, T. Ishikawa, T. Yamaguchi, and E. Lauga, *Phys. Fluids* **23**, 111702 (2011).
- [50] D. Saintillan and M. J. Shelley, *Phys. Rev. Lett.* **99**, 058102 (2007).
- [51] J. Stenhammar, R. Wittkowski, D. Marenduzzo, and M. E. Cates, *Phys. Rev. Lett.* **114**, 018301 (2015).
- [52] E. Lauga and T. R. Powers, *Rep. Prog. Phys.* **72**, 096601 (2009).
- [53] H. Diamant, *J. Phys. Soc. Jpn.* **78**, 041002 (2009).

Supplemental Material for “Enhanced hydrodynamic diffusion in dense binary active suspensions”

Zhouyang Ge^{1,2}, Shervin Bagheri¹, and Gwynn J. Elfring²

¹*FLOW, Department of Engineering Mechanics,*

KTH Royal Institute of Technology, 100 44 Stockholm, Sweden and

²*Department of Mechanical Engineering and Institute of Applied Mathematics,*

University of British Columbia, Vancouver V6T 1Z4, BC, Canada

CONTENTS

I. Models and methods	2
A. The squirmer model	2
B. Fast Stokesian Dynamics	3
C. Solver verifications	4
II. Results	6
A. Simulation set-up	6
B. Governing parameters	8
C. Spatial and energy distributions	8
D. Translational dynamics	11
E. Global nematic order	14
F. Spatial correlations	15
G. Toy model	17
References	18

I. MODELS AND METHODS

A. The squirmer model

In the main article, we briefly introduced the squirmer model. Here, we provide some additional details. The tangential slip velocity on the surface of a spherical squirmer may be expressed as [1]

$$\mathbf{u}_s = \sum_{n=1}^{\infty} \frac{2}{n(n+1)} P'_n(\mathbf{p} \cdot \mathbf{r}) [B_n(\mathbf{I} - \mathbf{r}\mathbf{r}) \cdot \mathbf{p} + C_n \mathbf{p} \times \mathbf{n}], \quad (\text{S.1})$$

where \mathbf{p} is a unit vector along the particle axis, \mathbf{r} the unit normal vector on the surface, P_n the Legendre polynomial of degree n , and $P'_n(x) = \partial P_n(x)/\partial x$. Note that, both \mathbf{u}_s and P_n are functions of $\mathbf{p} \cdot \mathbf{r}$.

From Eq. (S.1) we can observe two modes of motion: the B_n 's are the so-called squirmering modes, which gives rise to the longitudinal velocities about \mathbf{p} (such as the self-propulsion and self-straining); and the C_n 's are associated with azimuthal slip velocities about \mathbf{p} (such as the self-spin). As mentioned in the main article, it is customary to neglect all C_n 's while only keeping the two leading-order squirmering modes. Figure 1 shows the local slip velocity due to B_1 and B_2 , respectively, as well as the far-field stresslet flow due to B_2 (see the Supplementary Information of Ref. [2] for the far-field flow patterns of a few higher-order moments). Note the *asymmetry* of the flow intensity in the axis and perpendicular directions

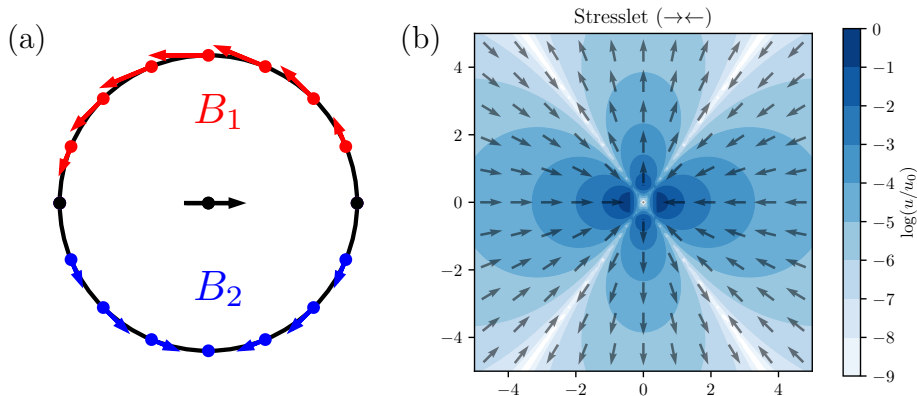


Figure 1: (a) Slip velocity on a squirmer due to either B_1 (red) or B_2 (blue). (b) The far-field stresslet flow due to B_2 (arrows indicate direction while color the magnitude). In both cases, the squirmer is oriented horizontally to the right.

due to mass conservation in three dimensions (the flow field is axisymmetric around \mathbf{p}); in two dimensions, the axis and perpendicular directions are symmetric, i.e. the velocity is zero along 45 degrees. Because pullers and pushers only differ in the sign of B_2 (thus the velocity direction in Figure 1b) in the squirmer model, the preferential orientation of two nearby pulling shakers is different from that of two pushing shakers: the former is more stable if they are aligned in the *axial* direction (i.e. head-to-head), whereas the latter in the *perpendicular* directions (i.e. side-by-side). This explains the anisotropic near-field distributions of pullers and pushers observed in our simulations; c.f. Figure 12 in the supplemental material.

B. Fast Stokesian Dynamics

The results in the main article were obtained from large-scale hydrodynamic simulations using the Fast Stokesian Dynamics (FSD) method [3], modified to include particle activities according to the active Stokesian Dynamics (SD) framework [1]. Below, we briefly describe the mathematical formulation of active SD and its implementation in FSD. Full details of the respective methods are available in Refs. [1, 3].

The dynamics of active suspensions can be formulated as follows. Assuming small, inertialess particles swimming in a viscous fluid at low Reynolds numbers, the external forces and torques on any particle must be balanced by their hydrodynamic counterparts, which can be linearly related to the velocity moments on the particle through a hydrodynamic resistance tensor. In the absence of external flow and Brownian motion, this leads to

$$\begin{pmatrix} \mathbf{U} \\ \mathbf{\Omega} \end{pmatrix} = \begin{pmatrix} \mathbf{U}_s \\ \mathbf{\Omega}_s \end{pmatrix} + \mathbf{R}_{\text{FU}}^{-1} \cdot \left[\begin{pmatrix} \mathbf{F}_{\text{ext}} \\ \mathbf{T}_{\text{ext}} \end{pmatrix} - \mathbf{R}_{\text{FE}} : \mathbf{E}_s \right], \quad (\text{S.2})$$

where \mathbf{U} and $\mathbf{\Omega}$ are, respectively, the linear and angular velocities of the particle, \mathbf{U}_s , $\mathbf{\Omega}_s$ and \mathbf{E}_s the respective self-propulsion, self-rotation and self-strain-rate, \mathbf{F}_{ext} and \mathbf{T}_{ext} the external force and torque (which may be zero), and \mathbf{R}_{FU} and \mathbf{R}_{FE} the resistance tensors coupling the force and velocity moments. Note that, both \mathbf{R}_{FU} and \mathbf{R}_{FE} depend only on the positions and orientations of the particles, thus the velocities can be computed quasi-statically to evolve the suspension. Finally, the same relationship also holds for passive particles; in that case, \mathbf{U}_s , $\mathbf{\Omega}_s$, and \mathbf{E}_s are all zero.

Numerically, we solve a modified form of Eq. (S.2) using FSD [3]. As in the conventional

SD [4], FSD decomposes the hydrodynamic resistance into a far-field and a near-field part,

$$\mathbf{R}_{\text{FU}} = \mathcal{B}^T (\mathcal{M}^{\text{ff}})^{-1} \mathcal{B} + \mathbf{R}_{\text{FU}}^{\text{nf}}, \quad \mathbf{R}_{\text{FE}} = \mathcal{B}^T (\mathcal{M}^{\text{ff}})^{-1} \mathcal{C} + \mathbf{R}_{\text{FE}}^{\text{nf}}, \quad (\text{S.3})$$

where \mathcal{M}^{ff} is the mobility tensor relating far-field force moments, $\mathcal{F}^{\text{ff}} \equiv (\mathbf{F}^{\text{ff}} \ \mathbf{T}^{\text{ff}} \ \mathbf{S}^{\text{ff}})^T$, to the velocity moments, $\mathcal{U} \equiv (\mathbf{U} \ \boldsymbol{\Omega} \ \mathbf{E})^T$, through mapping tensors \mathcal{B} and \mathcal{C} ,

$$\mathcal{B} \begin{pmatrix} \mathbf{U} \\ \boldsymbol{\Omega} \end{pmatrix} + \mathcal{C} \mathbf{E} = \mathcal{U}, \quad \mathcal{B}^T \mathcal{F}^{\text{ff}} = \begin{pmatrix} \mathbf{F}^{\text{ff}} \\ \mathbf{T}^{\text{ff}} \end{pmatrix}. \quad (\text{S.4})$$

After some algebra, Eq. (S.2) can then be reformulated as

$$\begin{bmatrix} \mathcal{M}^{\text{ff}} & \mathcal{B} \\ \mathcal{B}^T & -\mathbf{R}_{\text{FU}}^{\text{nf}} \end{bmatrix} \cdot \begin{bmatrix} \mathcal{F}^{\text{ff}} \\ \mathbf{U}_* \end{bmatrix} = \begin{bmatrix} -\mathcal{C} \mathbf{E}_s \\ \mathbf{F}_* \end{bmatrix}, \quad (\text{S.5})$$

with the short-hand notation

$$\mathbf{U}_* = \begin{pmatrix} \mathbf{U} - \mathbf{U}_s \\ \boldsymbol{\Omega} - \boldsymbol{\Omega}_s \end{pmatrix}, \quad \mathbf{F}_* = - \begin{pmatrix} \mathbf{F}_{\text{ext}} \\ \mathbf{T}_{\text{ext}} \end{pmatrix} + \mathbf{R}_{\text{FE}}^{\text{nf}} : \mathbf{E}_s. \quad (\text{S.6})$$

This can be verified by substituting Eqs. (S.3, S.4, S.6) into Eq. (S.5) to recover Eq. (S.2).

Eqs. (S.5, S.6) are the governing equations of the active FSD. They can be solved efficiently using the numerical procedure developed in the original FSD on a graphical processing unit. Once \mathbf{U} and $\boldsymbol{\Omega}$ are obtained, the particle positions and orientations are integrated forward in time using the standard or stochastic second-order Runge-Kutta method [5]. The source code of our implementation (including bug fixes of the original FSD solver) is available at <https://github.com/GeZhouyang/FSD>.

C. Solver verifications

The base solver of FSD was developed and verified to some extent by its original developers, Fiore and Swan [3]. Here, we present two additional verifications that are relevant to our physical problem. Specifically, we simulated two cases involving a pair of particles where analytical or numerical solutions were available previously. For validations of more

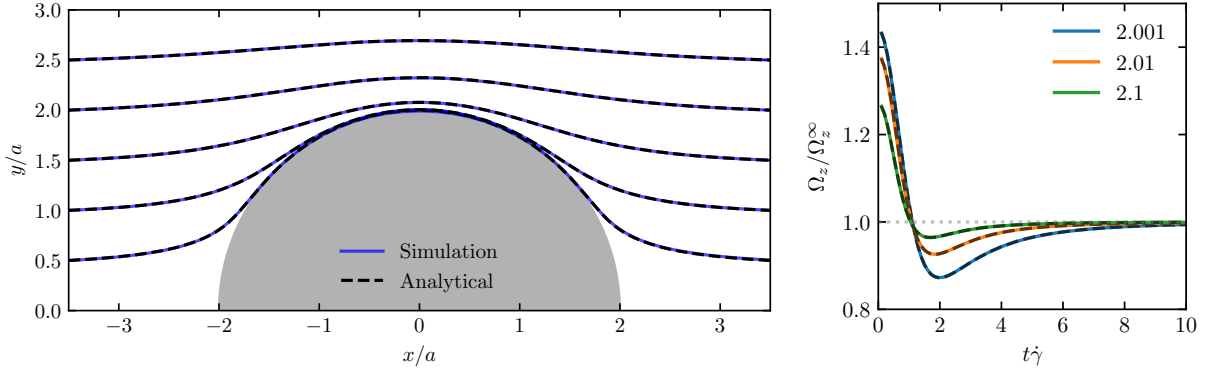


Figure 2: Relative trajectories of two passive spheres in the xy plane (left) and their angular velocity Ω_z (right) in simple shear flow, where a is the particle radius, $\dot{\gamma}$ the shear rate, and $\Omega_z^\infty = \dot{\gamma}/2$ the angular velocity of the flow. The different curves in the right figure correspond to the three initial conditions, $y_{min}/a = 2.001, 2.01,$ and 2.1 . The analytical solutions (dashed lines) are due to Batchelor and Green [7].

complex cases, such as the rheology of dense suspensions, see Ref. [6].

Figure 2 shows the relative trajectories of two passive particles of radius a in simple shear flow, in comparison to the analytical solutions of Batchelor and Green [7]. Here, the trajectories are fore-aft symmetric in the absence of non-hydrodynamic interactions or particle roughness. The interparticle gaps are minimal at $x = 0$ when the two particles are aligned in the velocity gradient direction. The excellent agreement between the simulation and the analytical solution verifies the numerical calculations of hydrodynamic interactions (HIs), in both short and long ranges. Furthermore, the angular velocities of the particles, though not affecting the translational motion of passive spheres, are also validated. This is a crucial check of the numerics, as the dynamics of active particles mainly depend on their orientations.

Figure 3 shows the velocity of a passive particle as a function of distance away from an active particle, in comparison to the analytical and numerical results of Ishikawa et al. [8]. Here, the translational velocity is decomposed into a radial and an azimuthal component, where both of them, as well as the angular velocity, are normalized by the appropriate squirmer modes (B_1 or B_2). As described in Ref. [8], the analysis of a passive particle next to an active one is sufficient for obtaining the result of two active particles, since the latter can be generalized from the former. We compare our simulation results with the far-field approximations and boundary element simulations (if available) of Ref. [8] in two cases: the active particle is (i) a puller with $\beta \equiv B_2/B_1 = 1$ and (ii) a shaker with $\beta = +\infty$. In

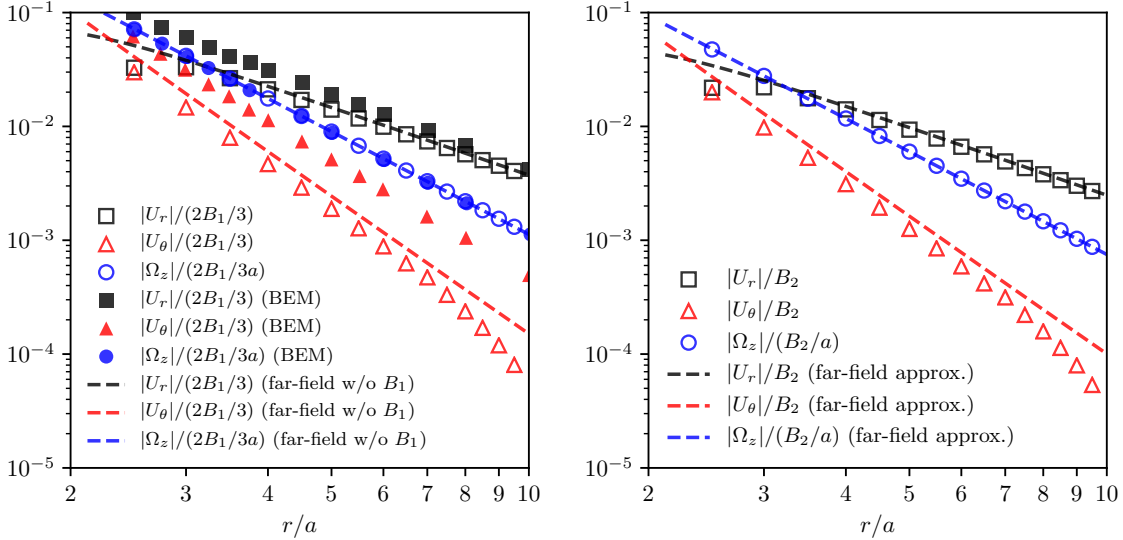


Figure 3: Velocity of a passive particle as a function of distance, r/a , next to an active particle, in comparison to the analytical and numerical results of Ishikawa et al. [8]. Here, the passive particle is at 45 degree from the active particle (left: puller with $\beta = 1$; right: shaker with $\beta = +\infty$); U_r and U_θ are the radial and azimuthal velocity components, while Ω_z is the only non-zero angular velocity; cf. Figure 5 in Ref. [8].

general, we observe good agreement between our and previous results, especially in terms of the angular velocity (Ω_z) and in the shaker case. The translational velocities we obtain are closer to the far-field solutions, which are slightly lower than the results from boundary element simulations. This deviation is expected since the entrainment effect due to B_1 (which decays as $1/r^3$ in three dimensions) is neglected in the current implementation to exploit the computational efficiency of FSD. However, the qualitative behavior and the scaling of the velocity with respect to distance are consistent with previous calculations.

II. RESULTS

A. Simulation set-up

We simulated binary suspensions in various compositions (in terms of the type of particle) and proportions (in terms of their mixing fraction); see Table I for a summary. Although we mostly reported the results of active-passive mixtures, (S_+, P) and (S_-, P) , at $\phi = 40\%$ and $N = 4096$ (cases 1 and 6) in the main article, the full simulations contain results of a smaller sample size ($N = 1024$), active-active mixtures (cases 7 and 8), and $\phi = 50\%$ (cases 8–10).

Case	ϕ	N	Group 1	Group 2	β_1	Pe_r
1	40%	4096	S ₊	P	$+\infty$	$+\infty$
2	40%	1024	S ₊	P	$+\infty$	$+\infty$
3	40%	1024	S ₊	P	$+\infty$	0.01
4	40%	1024	M	P	0	0
5	40%	1024	S ₋	P	$-\infty$	$+\infty$
6	40%	4096	S ₋	P	$-\infty$	$+\infty$
7	40%	1024	S ₊	S ₋	$+\infty$	$+\infty$
8	50%	1024	S ₊	S ₋	$+\infty$	$+\infty$
9	50%	1024	S ₊	P	$+\infty$	$+\infty$
10	50%	1024	S ₋	P	$-\infty$	$+\infty$

Table I: Summary of the simulations. ϕ and N are the total volume fraction and number of particles, respectively. Each suspension contains two groups of particles at various proportions: pulling shakers (S₊), pushing shakers (S₋), neutral movers (M), and passive spheres (P). β_1 and Pe_r are, respectively, the squirmer parameter and Péclet number based on the rotational noise of particles in group 1. β_2 can be defined similarly.

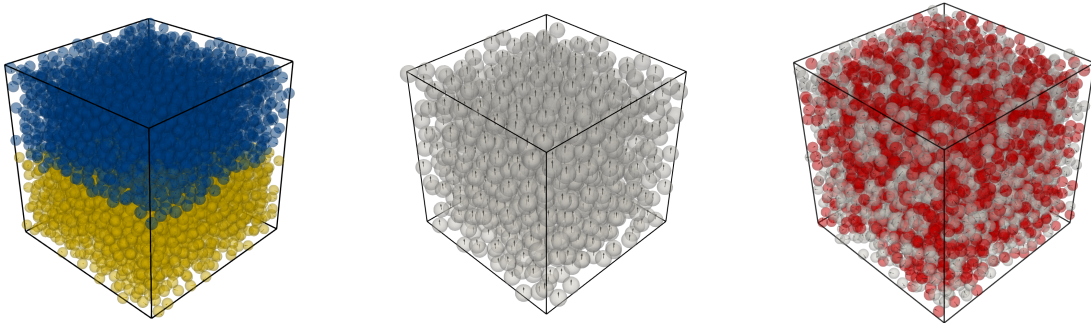


Figure 4: Examples of three different initial conditions, where the color represents the type of particle and the arrow denotes the particle orientation.

In all but two cases (3 and 4) the rotational dynamics of the active particles were governed by HIs alone; in case 3 we imposed a strong noise in the angular velocities (see the main article), and in case 4 we suppressed the HIs due to particle activity entirely. Comparison between cases 1 and 2 as well as 5 and 6 showed no qualitative difference in the statistical results, thus the number of particles were mostly set to $N = 1024$. Computationally, each simulation was performed in cubic domains with periodic boundary conditions; different initial conditions (in terms of the particles' position and orientation, see Figure 4) were also tested and had no effect on the steady-state results.

B. Governing parameters

The control parameter in each case is the fraction of particles in the second group, termed f_p in the main article since we were focusing on the effect of passive particles. f_p was varied between 0 and 1 with smaller increments near 0. In principle, one could also vary the strength of the second squirming mode, B_2 , to examine the potential rate dependence of the global dynamics; c.f. Ref. [9]. However, we fixed $|B_2|$ to reduce the number of parameters. Numerically, it is customary to impose a short-range repulsive force to prevent the particles from overlapping. Here, we used the electrostatic repulsion typical for colloids, viz. $F_{ext} = F_0 \exp(-\kappa h)$, where F_0 is the maximal repulsion, κ the inverse Debye length, and h the surface gap between two particles [10]. These allow us to define two time scales, $\tau_a \equiv a/|B_2|$ and $\tau_e \equiv 6\pi\eta a^2/F_0$. Throughout this work we fixed $\tau_e/\tau_a = 0.02$ and $\kappa^{-1}/a = 0.01$ to model a strong, short-range repulsion. This choice is consistent with our previous work on passive suspensions [6].

C. Spatial and energy distributions

In the main article, we showed the spatial and energy distributions of the (S₊,P) suspension at $f_p = 0.5$ (case 1), claiming that the former is random and the latter equally shared among the two particle groups. Here, we provide more details in support of those claims.

Figure 5 shows the probability $\rho_k^{(ij)}$ of a particle in group i to find its first k nearest neighbors to be all in group j , as introduced in the main article. Specifically, the top row is the (S₊,P) suspension with $f_p = 0.5$ (case 1), the bottom row the (M,P) suspension with $f_p = 0.5$ (case 4); the left column shows the temporal evolutions of these probabilities, the right column their steady-state values. The behaviors for (S₋,P) suspensions as well as those at $\phi = 50\%$ are similar to case 1. We note that there is a slight bias for passive particles (group 2) to be closest to active ones (more so for pushers than pullers), as $\rho_{k=1}^{(21)} > 0.5$. In the shaker case, this bias may be attributed to the attractive stresslet flow induced by an active particle in its axial or perpendicular direction (c.f. Figure 1b), which is absent between passive spheres. In the mover case, the bias is due to the directed motion – it is more likely for a passive particle to be hit by (thus close to) an active mover than another passive particle. However, the main difference between the top and bottom rows of Figure

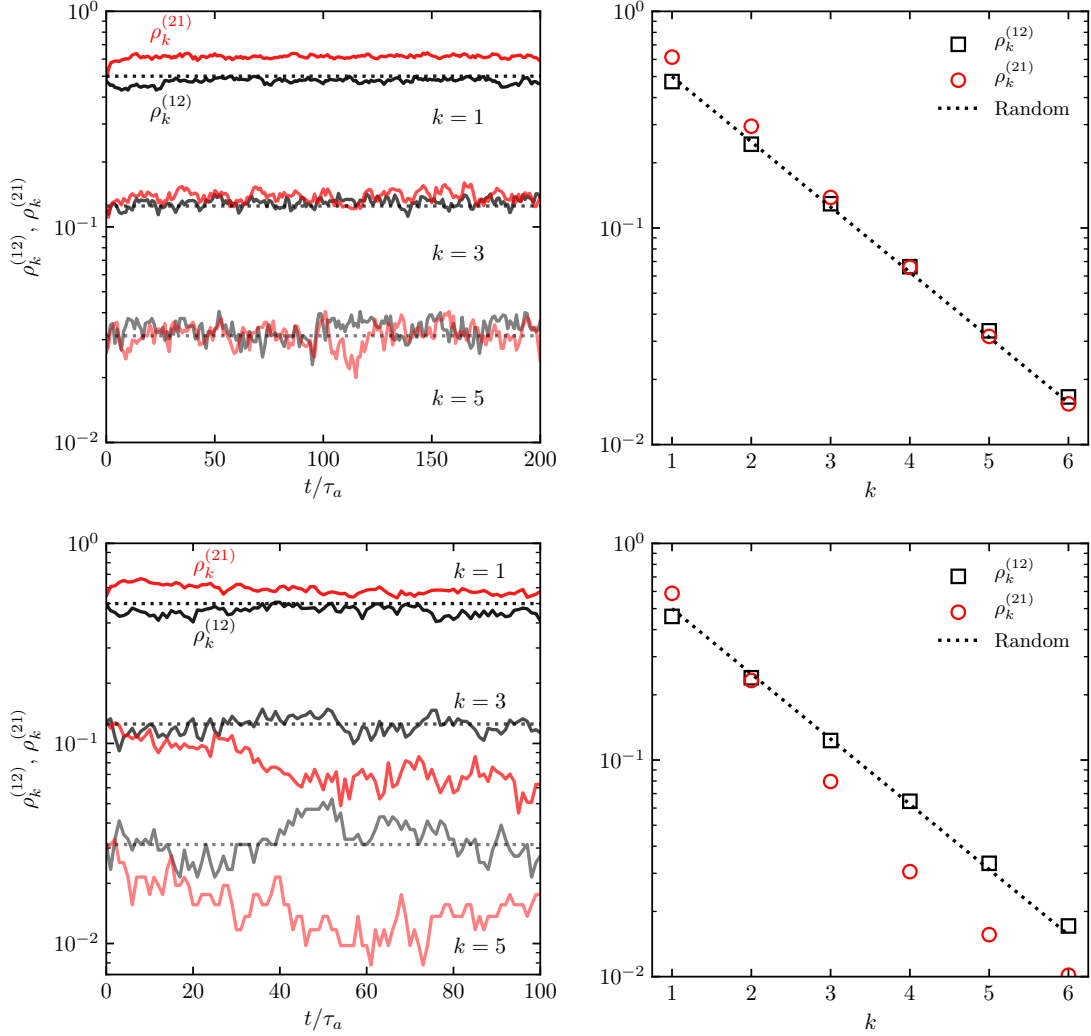


Figure 5: Probability $\rho_k^{(ij)}$ of a particle in group i to find its first k nearest neighbors to be all in group j ; top row: the (S₊,P) suspension with $f_p = 0.5$ (case 1); bottom row: the (M,P) suspension with $f_p = 0.5$ (case 4). Dotted lines correspond to random mixtures.

5 lies in $\rho_k^{(ij)}$ for $k \geq 3$. Clearly, a passive particle is less likely to be surrounded by a self-propelling mover than what would be expected in a random configuration, whereas the probability remains random with increasing k in the shaker case.

Figure 6 shows the root mean square translational (U_{rms}) and angular (Ω_{rms}) velocities in (S₊,P) and (S₋,P) suspensions under three different f_p 's. As mentioned in the main article, both U_{rms} and Ω_{rms} are approximately the same in the two particle groups, regardless of the composition and mixing fraction. Note that, suspensions of pulling shakers are more energetic than pushing shakers, consistent with their long-time diffusivities; c.f. Figure 2(b) in the main article. This is probably because pulling shakers tend to be aligned along their

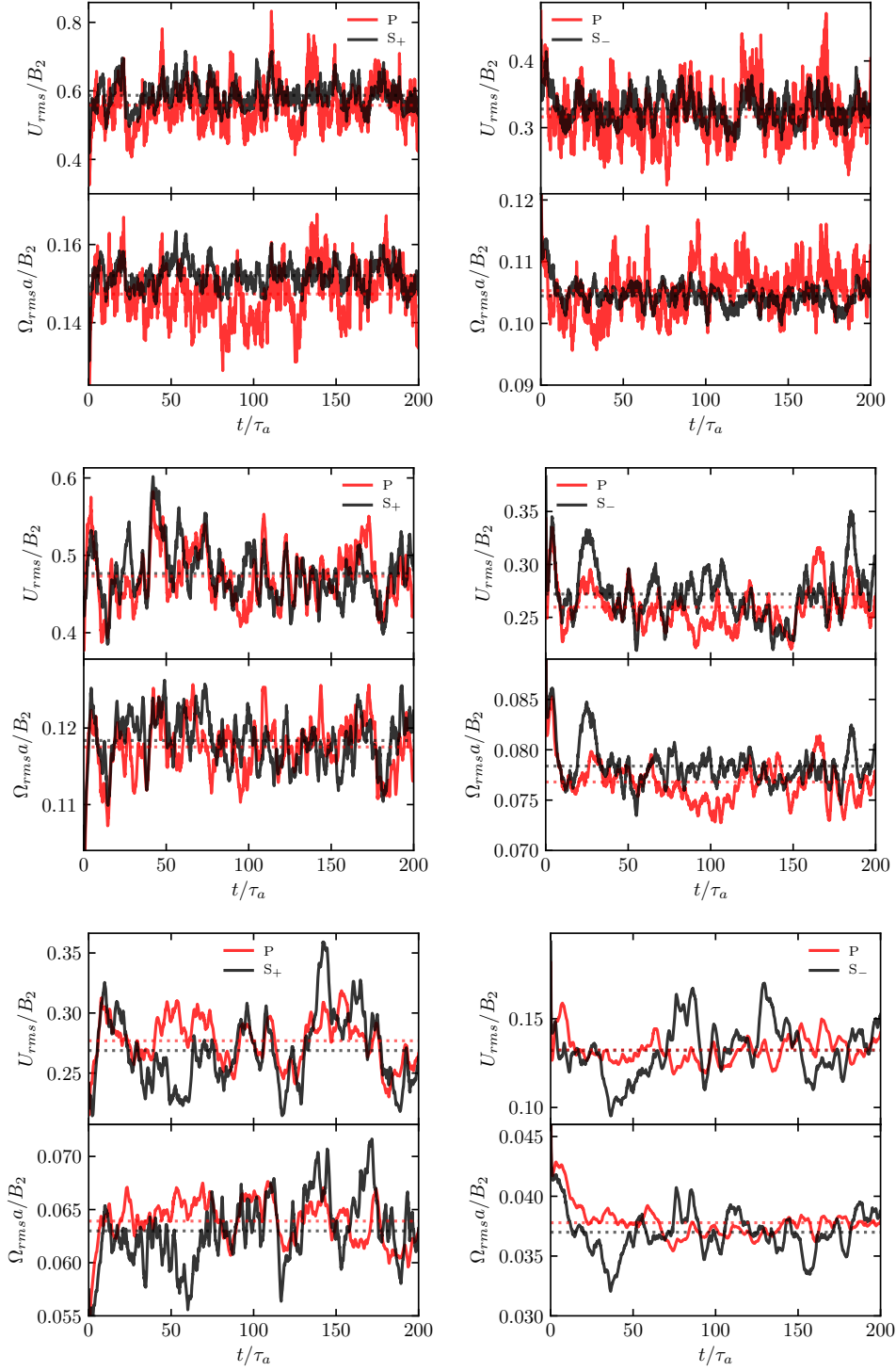


Figure 6: Root mean square translational (U_{rms}) and angular (Ω_{rms}) velocities in time, where $\tau_a = a/B_2$. Left column: (S_+, P) suspensions (case 1); right column: (S_-, P) suspensions (case 6). Top row: $f_p = 0.1$; middle row: $f_p = 0.5$; bottom row: $f_p = 0.9$. Dotted lines are the mean.

own axes, where the induced stresslet flow is stronger than in the perpendicular directions; then, replacing a shaker with a passive particle will lead to larger net flow (c.f. the toy model in the main article). Note also that the results are noisier if they are averaged over less particles (red lines in the top row and black lines in the bottom row). Nevertheless, their mean values are roughly the same between the two groups, and we consistently observe $U_{rms} > \Omega_{rms}a$, indicating the violation of the equipartition theorem.

D. Translational dynamics

In the main article, we showed the rescaled mean square displacements (MSD), $\langle \Delta r^2(t) \rangle / 6Dt_c$, based on the model of Wu and Libchaber [11]; c.f. Figure 2(a) in the main article. Figure 7(a) shows the raw MSDs, which crossover from ballistic to diffusive dynamics around time t_c . Although the ballistic dynamics persist for more than a few τ_a , the distributions of the displacements all have finite variances, thus the dynamics will eventually become diffusive according to the central limit theorem; see Figure 7(a) inset. Figure 7(b) shows the cumulative probability density function (CDF) of the particle displacements in the z direction over a short time $t = \tau_a$ in the ballistic regime (the CDFs in x and y are similar). These CDFs are generally well fitted by the error functions, except for the case at $f_p = 0.99$, where the suspension is mostly passive. However, even in that case, the CDF, \mathcal{C} , quickly converges to 1 for large displacement, Δs , as $1 - \mathcal{C}(\Delta s) \sim \Delta s^{-2}$ at least (thus the probability density function, PDF, decays as Δs^{-3} at least); see the inset of Figure 7(b). Indeed, direct inspection of the PDFs shows that the data are well fitted by either the Gaussian distribution or an alternative form proposed by Leptos et al. [12],

$$\mathcal{P}(\Delta x) = \frac{1-f}{\sqrt{2\pi}\delta_g} e^{-\Delta x^2/2\delta_g^2} + \frac{f}{2\delta_e} e^{-|\Delta x|/\delta_e}, \quad (\text{S.7})$$

where δ_g is the standard deviation of the Gaussian core, δ_e the exponential decay length, and f the fraction of the enhanced displacements. The variance is finite in either case. However, we note that the exponential decay at $f_p = 0.99$ is probably a transient behavior due to the poor statistics (not enough active particles in the sample) [13].

Figure 8 shows the translational dynamics in short and long times of the binary suspensions for all cases. Here, we define the relative short-time dynamics, σ^2/σ_0^2 , as the ratio of

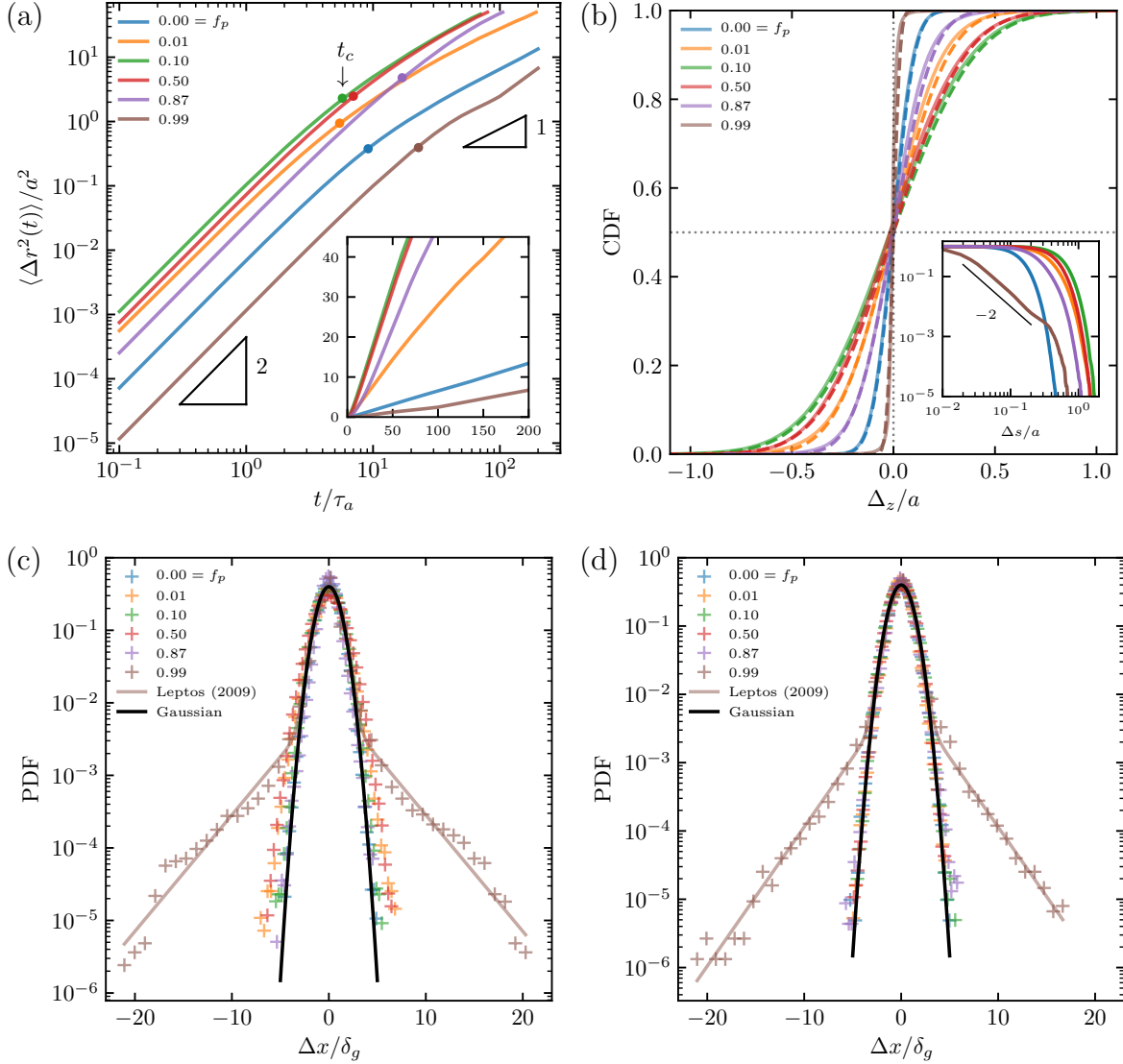


Figure 7: Statistics of the particle displacements in (S_+,P) suspensions (a–c) and (S_-,P) suspensions (d) at $\phi = 40\%$, $N = 4096$. (a) MSD in time, showing crossover from ballistic (slope 2) to diffusive (slope 1) dynamics, with crossover time t_c (c.f. Figure 2(a) in the main article). Inset shows the same data on linear scales. (b) Cumulative probability density function (CDF) of the particle displacements in the z direction (similarly in x and y) over $t = \tau_a$. The full lines are from the simulations and the dashed lines are their Gaussian fits. Inset shows the decay of $1 - \mathcal{C}(\Delta s)$, where \mathcal{C} denotes the CDF and Δs is the scalar net displacement. (c,d) Probability density function (PDF) of the particle displacements in x direction over $t = \tau_a$, normalized by the standard deviation of the Gaussian core, δ_g ; (S_+,P) suspensions in (c) and (S_-,P) suspensions in (d). Data at $f_p = 0.99$ are better fitted by Eq. (S.7) as in Leptos et al. [12], though the exponential tail is probably a transient phenomenon [13].

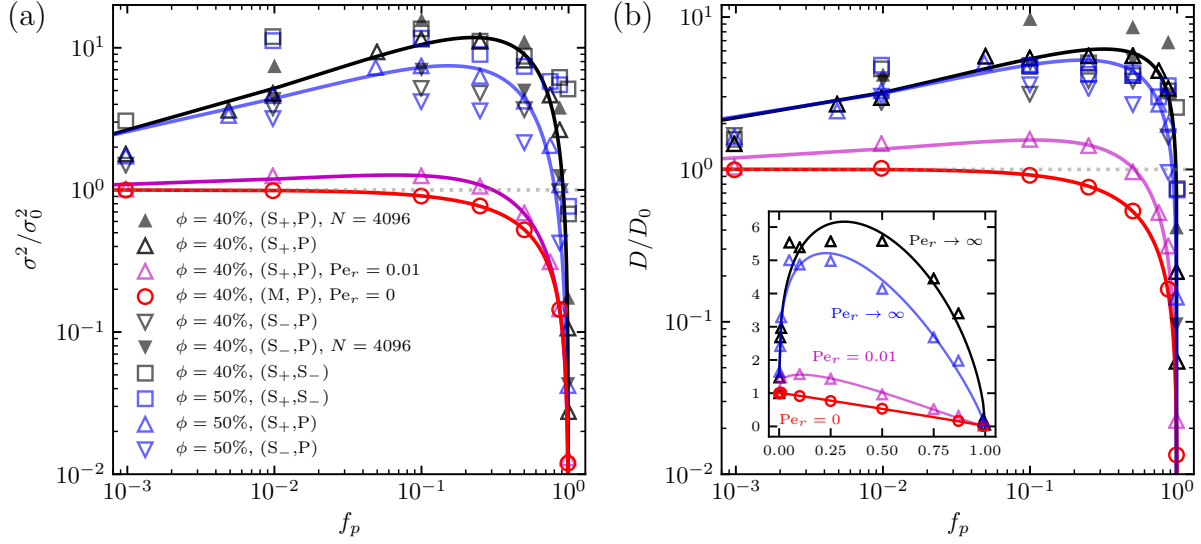


Figure 8: Relative short-time dynamics (a) and long-time diffusivity (b) of the binary active suspensions. σ^2 is the MSD per unit time (in τ_a) and D is the diffusion coefficient extracted from the MSD as described in the main article; their values at $f_p = 0$ are denoted by the subscript zero. In both plots, lines are least squares fits of the form $y = ax^{\nu_1}(1-x)^{\nu_2} + 1 - x$. The inset in (b) shows four representative cases on linear scales.

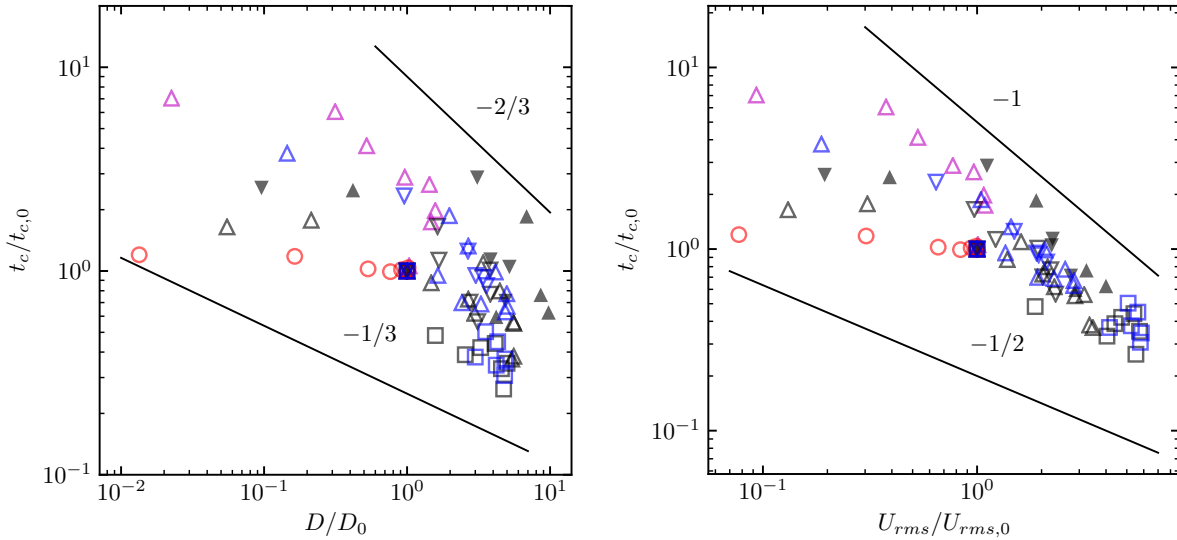


Figure 9: Correlations between the crossover time t_c and the diffusivity D as well as U_{rms} .

the MSDs per unit time at a finite f_p and $f_p = 0$, and the relative long-time diffusivity, D/D_0 , same as in the main article. Clearly, the dynamics in both short and long times can be significantly enhanced in the presence of a small fraction of passive particles. This applies to both (S₊,P) and (S₋,P) suspensions, as well as the (S₊,S₋) suspensions, as $Pe_r \rightarrow \infty$. We note that the dynamics enhancement is stronger in the short time than in the long

time (nevertheless, they are positively correlated; c.f. Figure 2(c) in the main article). This implies that there is only one timescale in our dynamics, which originates from the HIs. Furthermore, the correlation between t_c and D (and also U_{rms}) must be negative, since on dimensional ground one expects $D \sim U_{rms}^2 t_c$. Indeed, we observe $t_c \sim D^{-\nu_1}$ and $t_c \sim U_{rms}^{-\nu_2}$, with $1/3 \leq \nu_1 \leq 2/3$ and $1/2 \leq \nu_2 \leq 1$, see Figure 9. Despite the large scatter of the data (likely due to uncertainties in estimating D and t_c), the lower bounds of these exponents are consistent with the observed $D \sim U_{rms}^{1.5}$ scaling, c.f. Figure 2(c) in the main article. Overall, the dynamics enhancement in binary suspensions of shakers is robustly observed, i.e., it is not sensitive to the volume fraction, sample size, or type of shakers.

E. Global nematic order

In the main article, we mentioned that the orientations of the shakers at steady state are isotropic in our binary suspensions. Below, we provide explicit evidence supporting this claim.

Since shakers have $\mathbf{n} \rightarrow -\mathbf{n}$ symmetry, we calculate the nematic tensor, \mathbf{Q} , defined as

$$Q_{ij} = \frac{3}{2} \left(\langle n_i n_j \rangle_1 - \frac{1}{3} \delta_{ij} \right), \quad (\text{S.8})$$

where $\langle \cdot \rangle_1$ denotes the average over all particles in the first group. By definition, \mathbf{Q} is symmetric and traceless, and its largest eigenvalue, λ , measures the nematic order: $\lambda = 0$ if the system is isotropic; $\lambda = 1$ if it is maximally nematic [14]. Figure 10 shows the time evolution of λ and its mean value λ_m at steady state. Clearly, there is no nematic order in all cases as λ_m is always negligible regardless of f_p , the combination of particles, and their initial conditions. Note that, the increase of λ_m as $f_p \rightarrow 1$ is due to the finite sample size. By central limit theorem, $|\lambda_m - \bar{\lambda}| \sim \sigma_\lambda / \sqrt{N(1 - f_p)}$, where $\bar{\lambda}$ and σ_λ are the true mean and standard deviation of λ_m , respectively. If the suspension was isotropic (i.e. $\bar{\lambda} = 0$), we would expect $\lambda_m \sim 1 / \sqrt{N(1 - f_p)}$, which is indeed the case as shown in Figure 10 (see the inset of Figure 10a). This is also true for the second particle group, if it is composed of active particles. Therefore, our data show that shakers remain isotropically oriented in the presence of passive particles.

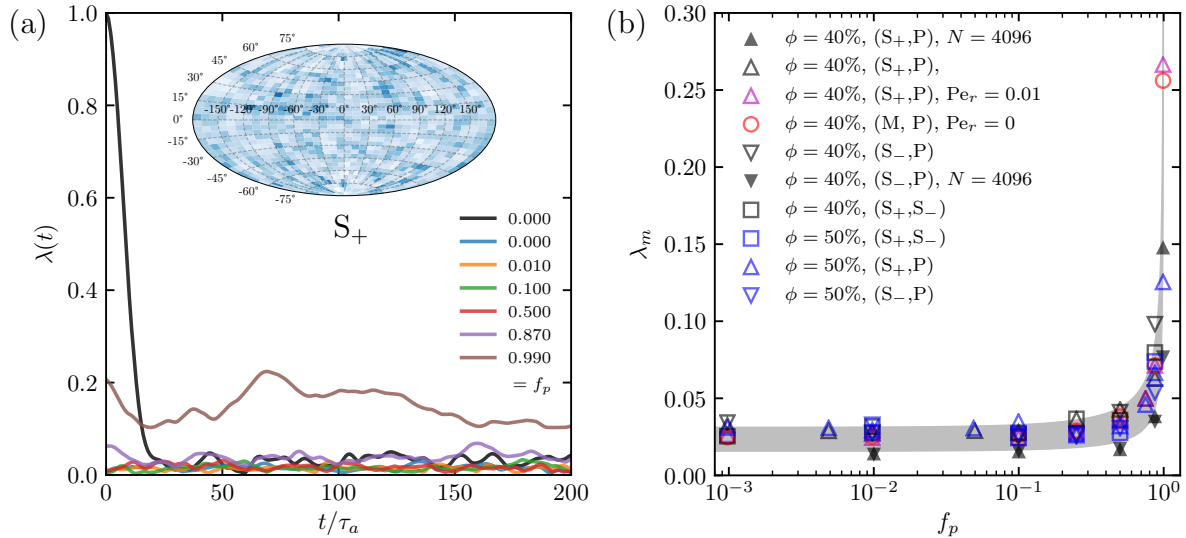


Figure 10: Global nematic order. (a) Time evolutions of the nematic order λ of (S_+,P) suspensions at $\phi = 40\%$ ($N = 4096$); inset shows the orientation distribution (Aitoff projection) of $f_p = 0$ at steady state. (b) Mean nematic order λ_m of all cases. The shade corresponds to the standard error in the estimation of λ_m given a limited sample size.

F. Spatial correlations

In the main article, we showed an activity-induced local ordering of shakers; c.f. Figure 4 therein. As can be expected, the ordering is strongest at $f_p = 0$ (i.e., when there are only shakers in the suspensions) and will decrease with f_p , since the effect of passive particles on the orientation of other particles are weaker. Figure 11 shows the orientation correlation, $\langle |\mathbf{n}_0 \cdot \mathbf{n}_r| \rangle$, in (S_+,P) suspensions at $f_p = 0, 0.1$ and 0.5 . Here, the averaging is only over active particles as the orientation of passive spheres has no effect on the dynamics. Clearly, the distance over which the orientation of the shakers are correlated reduces with f_p . However, nearly touching shakers remain correlated even at $f_p = 0.5$ (further increasing f_p leads to large fluctuations in the results as the sample size becomes too small). This can also be seen in Figure 12, where we plot the angular distributions of pulling and pushing shakers in their own body frame at $f_p = 0.5$. Note that in these maps the reference particle is always active, whereas the neighbors can be either active or passive (since in the toy model we consider the effect of passive particles on an active lattice). The same patterns are observed at $f_p = 0.5$ and $f_p = 0$ (c.f. Figure 4(a) in the main article), thus the same local order and the same mechanism for enhanced hydrodynamic diffusion by passive particles are at play.

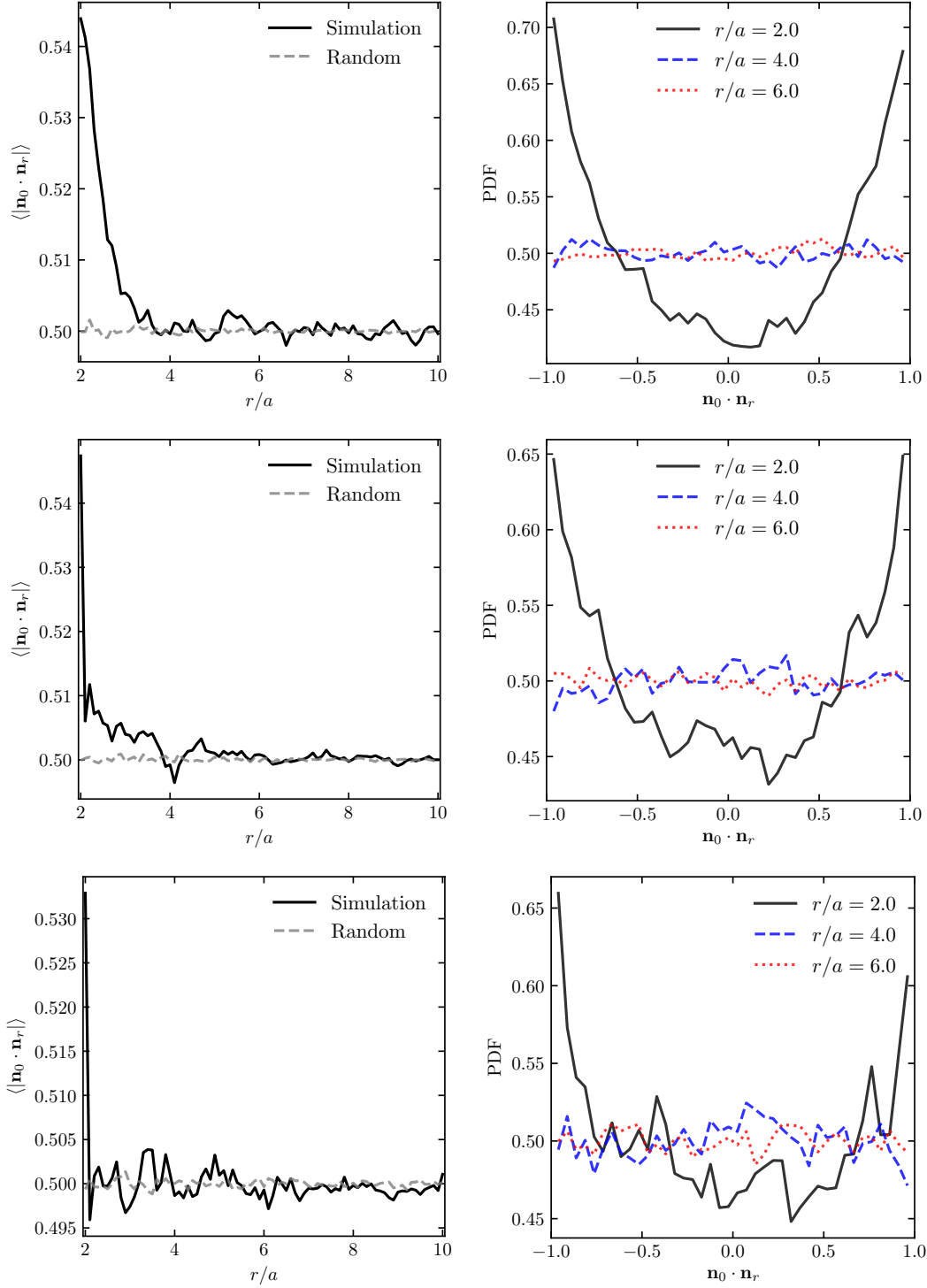


Figure 11: Orientation correlations in (S_+,P) suspensions at different f_p ($\phi = 40\%$, case 1). Left column: radial distributions of $\langle |\mathbf{n}_0 \cdot \mathbf{n}_r| \rangle$. Right column: probability density functions of $\mathbf{n}_0 \cdot \mathbf{n}_r$. Top row: $f_p = 0$. Middle row: $f_p = 0.1$. Bottom row: $f_p = 0.5$.

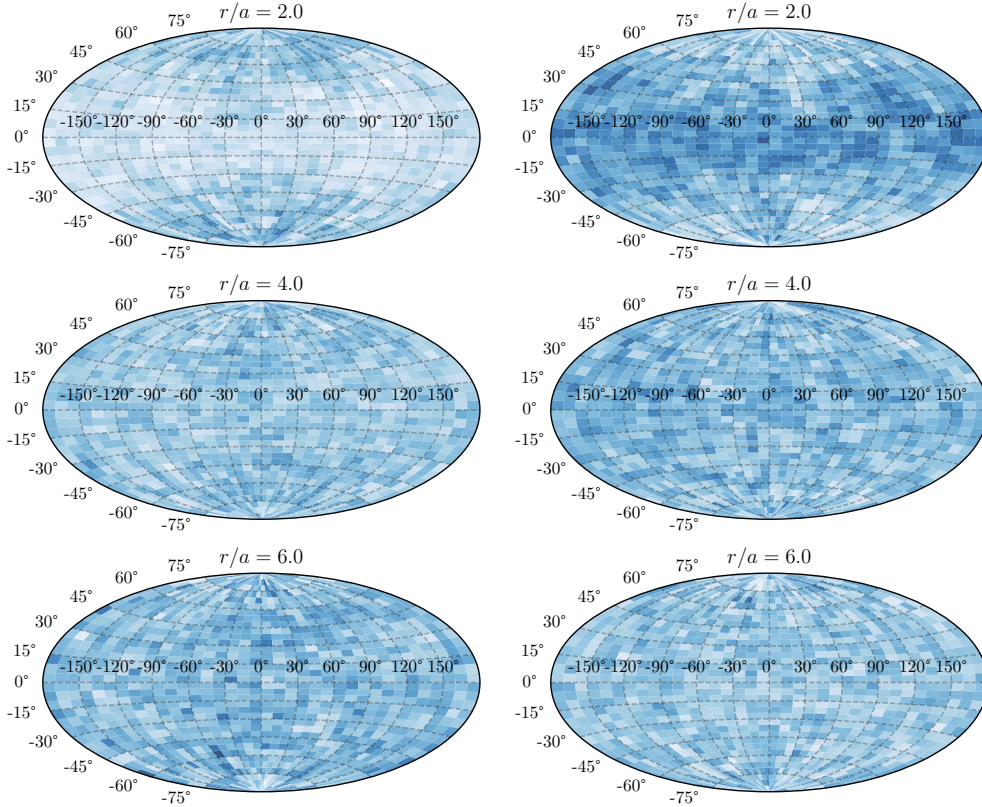


Figure 12: Angular distributions at three representative distances for suspensions of pulling (left) and pushing (right) shakers; $f_p = 0.5$, $\phi = 40\%$ (cases 1 and 6). Top row: $r/a = 2.0$; middle row: $r/a = 4.0$; bottom row: $r/a = 6.0$; c.f. Figure 11.

G. Toy model

In the main article, we illustrated the effect of passive particles on the dynamics of binary suspensions of shakers using a two dimensional square lattice, but mentioned that the same effect would be observed in any lattices with reflection and twofold symmetries, such as hexagonal or cubic lattices, because they preserve the symmetry of the stresslet flow. As an example, Figure 13 (left) shows the results on two dimensional hexagonal lattices, where alignment leads to nonmonotonic dynamics, with a peak at $f_p = 0.5$, and random orientations lead to monotonically decreasing dynamics with f_p . This is the same as in square lattices (see Figure 5(c) in the main article). The reason that the dynamics reduce with the amount of passive particles in randomly oriented lattices is because the induced flow therein is *additive* (i.e. it is more likely for the superimposed length of two randomly oriented vectors to be greater than any of the original one in two and higher dimensions). In Figure 13 (right) we also show the results on a square lattice, but with noise added in

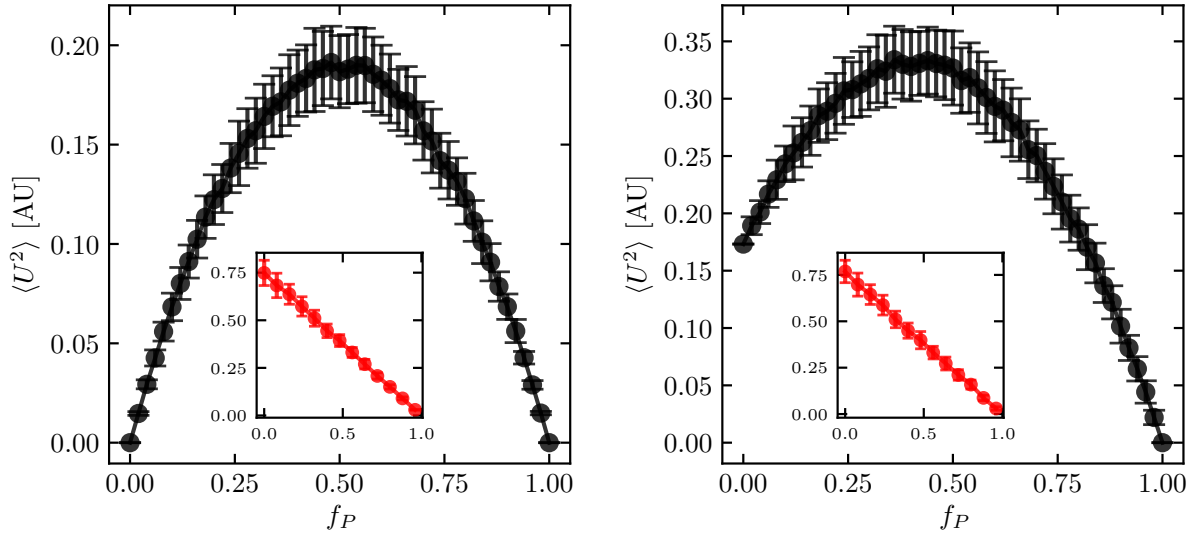


Figure 13: Mean square velocity in arbitrary units as a function of f_p obtained from 100 periodic lattices of 100 particles; the active particles are aligned in the main plots (black) but oriented randomly in the insets (red). Left: hexagonal lattices. Right: square lattices with noise in the particle position (similarly if noisy in the orientation).

the particle position (i.e. the particles do not perfectly sit on the lattice points). Clearly, the dynamics are nonmonotonic if the particles are aligned, and they resemble the actual observations better, since $\langle U^2 \rangle \neq 0$ at $f_p = 0$ and the peak occurs at a fraction $f_* < 0.5$; c.f. Figure 2(b) in the main article. Finally, we note that the results are essentially the same if a small amount of noise is added to the particle orientation.

-
- [1] G. J. Elfring and J. F. Brady, *J. Fluid Mech.* **952**, A19 (2022).
 - [2] A. J. Mathijssen, D. O. Pushkin, and J. M. Yeomans, *J. Fluid Mech.* **773**, 498 (2015).
 - [3] A. M. Fiore and J. W. Swan, *J. Fluid Mech.* **878**, 544 (2019).
 - [4] J. F. Brady and G. Bossis, *Ann. Rev. Fluid Mech.* **20**, 111 (1988).
 - [5] A. Iniesta and J. Garcia de la Torre, *J. Chem. Phys.* **92**, 2015 (1990).
 - [6] Z. Ge and G. J. Elfring, *Phys. Rev. E* **106**, 054616 (2022).
 - [7] G. Batchelor and J.-T. Green, *J. Fluid Mech.* **56**, 375 (1972).
 - [8] T. Ishikawa, M. Simmonds, and T. J. Pedley, *J. Fluid Mech.* **568**, 119 (2006).
 - [9] Z. Ge, R. Martone, L. Brandt, and M. Minale, *Phys. Rev. Fluids* **6**, L101301 (2021).
 - [10] J. Mewis and N. J. Wagner, *Colloidal suspension rheology* (Cambridge University Press, 2012).

- [11] X.-L. Wu and A. Libchaber, Phys. Rev. Lett. **84**, 3017 (2000).
- [12] K. C. Leptos, J. S. Guasto, J. P. Gollub, A. I. Pesci, and R. E. Goldstein, Phys. Rev. Lett. **103**, 198103 (2009).
- [13] J.-L. Thiffeault, Phys. Rev. E **92**, 023023 (2015).
- [14] M. Doi, *Soft matter physics* (Oxford University Press, USA, 2013).